frontiers
in Mechanical Engineering

ORIGINAL RESEARCH
published: 21 April 2021
doi: 10.3389/fmech.2021.642214

Investigation of Structure-Property-Boiling Enhancement Mechanisms of Copper/Graphene Nanoplatelets Coatings

Aniket M. Rishi[1,2]*, Seyed Alireza Rozati*[2]*, Carole Trybus*[3]*, Satish G. Kandlikar*[1,4] *and Anju Gupta*[2]*

[1]Microsystems Engineering, Rochester Institute of Technology, Rochester, NY, United States, [2]Department of Mechanical, Industrial and Manufacturing Engineering, University of Toledo, Toledo, OH, United States, [3]Materion Performance Alloys and Composites, Elmore, OH, United States, [4]Mechanical Engineering, Rochester Institute of Technology, Rochester, NY, United States

OPEN ACCESS

Edited by:
Ali Kosar,
Sabancı University, Turkey

Reviewed by:
Xili Duan,
Memorial University of Newfoundland, Canada
Osamu Kawanami,
University of Hyogo, Japan

****Correspondence:***
Anju Gupta
anju.gupta@utoledo.edu

Specialty section:
This article was submitted to Thermal and Mass Transport, a section of the journal Frontiers in Mechanical Engineering

Received: *15 December 2020*
Accepted: *15 February 2021*
Published: *21 April 2021*

Citation:
Rishi AM, Rozati SA, Trybus C, Kandlikar SG and Gupta A (2021) Investigation of Structure-Property-Boiling Enhancement Mechanisms of Copper/Graphene Nanoplatelets Coatings. Front. Mech. Eng 7:642214. doi: 10.3389/fmech.2021.642214

In this work, we present an exceptionally high heat transfer coefficient (HTC) and critical heat flux (CHF) achieved by graphene nanoplatelets (GNPs) and copper composite coatings with tunable surface properties. These coatings were created by a combination of powder metallurgy and manufacturing processes including ball milling, sintering, electrodeposition, and salt-patterning. We demonstrated correlations between various coating processes, resultant surface morphologies, properties, and improved boiling mechanism. Electrodeposition of GNP and copper particles led to formation of tall ridge-like structures and valleys to contain the boiling fluid in between. Higher CHF achieved for these coatings was attributed to the microlayer evaporation. It was observed that ball milling of GNP and copper particles prior to their sinter-coating enhanced their surface roughness that resulted in very high HTC, nearly 5.4 times higher than plain copper surfaces. Additional salt-patterning along with sinter-coating yielded interconnected porous networks with high nucleating activity that rendered record-breaking HTC of 1,314˚kW/m^2-˚C. Combination of these coating processes can be adopted to tailor the surfaces and achieve better boiling performance. Novel techniques developed in this work can be applied to a variety of thermal engineering applications.

Keywords: graphene nanoplatelets, powder metallurgy, high temperature coatings, functional surfaces, heat transfer coefficient

---

Abbreviations: CHF, critical heat flux (W/cm^2); D_d, vapor bubble departure diameter (m); dT, temperature gradient (˚C); f, bubble release frequency (numbers/second); HTC, heat transfer coefficient (W/m2-˚C); k_{Cu}, thermal conductivity of copper (W/m-K); q'', heat flux (W/cm^2); T_{wall}, surface temperature of the test section (˚C); ρ_l, density of liquid (kg/m³); ρ_v, density of vapor (kg/m³); g, acceleration due to gravity (m/s2); σ, surface tension of the liquid at saturation conditions (N/m); h_{fg}, latent heat of vaporization (J/kg); q, heat flux (W/m^2); V_d, velocity of the departing bubble (m/s).

INTRODUCTION

The mechanisms underlying enhanced pool boiling heat transfer have been investigated in past few decades for efficient design of reboilers (Thome, 1988; Lavrikov et al., 2015), heat exchangers (Antonelli and O'Neill, 1981; Ohta et al., 2004), power electronics (Kercher et al., 2003; Wei et al., 2009; Sadaghiani et al., 2017; Sinha-Ray et al., 2017; Zhang et al., 2018; Chauhan and Kandlikar, 2019), and other high temperature engineering applications (Konishi and Mudawar, 2015; Mudawar, 2017). This is attributed to high heat transfer efficiencies or heat dissipation exhibited by pool boiling due to the absorption of large amount of latent heat which is accompanied by phase change from liquid to vapor (Kandlikar, 2019; Amalfi et al., 2020). Numerous studies have improved the boiling performance by increasing the effective surface area through inclusion of micron scale enhancements such as pin-fins (Cao et al., 2018; Kong et al., 2018; Orman et al., 2019), microchannels (Cooke and Kandlikar, 2012; Walunj and Sathyabhama, 2018), notches (McLaughlin, 2019), and other micro and/or nanostructures (Yao et al., 2012; Kandlikar, 2013; Kandlikar, 2017; Raghupathi and Kandlikar, 2017; Yuan et al., 2019). Contoured fin structures cause the bubbles to sweep away from the fin tops resulting in higher bubble departure rates; thereby increasing the heat dissipation. Microchannel-based geometries enhance the boiling performance by creating a physical barrier that separates nucleating and non-nucleating regions, generating separate liquid and vapor pathways for the bubble departure and liquid re-entry (Kandlikar, 2013). The enhancements due to these channels are also due to the strong liquid currents forming over the feeder channels that suppresses the unwanted nucleation and allows separate vapor–liquid pathways that are functional at higher heat fluxes as well (Jaikumar and Kandlikar, 2016). Additionally, liquid jet impingement-based techniques have been implemented by other researchers as well to suppress nucleate boiling in unwanted regions and improve the resultant pool boiling performance (Jaikumar et al., 2017b; Yuan et al., 2019; Pi et al., 2020).

Modifications by varying surface geometries have shown to provide separate pathways for departing bubbles and the incoming liquid that result in higher critical heat fluxes. However, such enhancements create a thermal gradient across the height of the structures resulting in higher wall superheats. Functional surface coatings have also shown promising enhancements in pool boiling due to altered surface properties and structures that improve the overall functionality of the heater surfaces (Park et al., 2014; Patil and Kandlikar, 2014; Patil et al., 2014). It has been demonstrated that the functional surfaces with high porosity intensify the vapor bubble activity as a result of increased nucleation site density. Our previous works have established that the pool boiling critical heat flux (CHF) and heat transfer coefficients (HTC) increase significantly with respect to increased nucleation sites as a result of porosity (Rishi et al., 2018; Rishi et al., 2019a). We have also demonstrated a significant shift in the boiling curve toward lower wall superheat with graphene and copper-based coatings that possessed superior surface porosity, wettability, and wickability (Jaikumar et al., 2017c). These functional coating surfaces with hierarchical pores act as nucleation sites and further improve the vapor bubble dynamics (Gupta et al., 2018a; Rishi et al., 2019a). In addition to porosity, other surface parameters such as surface roughness, wettability, and wickability have also shown to improve the boiling performance by inducing capillary-based liquid resupply into the nucleation sites that delays the vapor layer formation. Carbon nanomaterial coatings, particularly graphene, and carbon nanotubes have been explored for boiling performances (Lee et al., 2016; Jaikumar et al., 2017b; Gupta et al., 2018a; Gajghate et al., 2020; Vasudevan et al., 2020); however, these coatings did not alter the heat fluxes and heat transfer coefficients, significantly. In our recent work, we extensively studied the pool boiling performance of multiscale coatings of graphene and graphene oxide that were produced through electrochemical exfoliation of graphite, and through chemical vapor deposition (Gupta et al., 2018a). We observed that microscale or multilayered graphene coatings performed better than the nanoscale coatings with one to three layers. The microscale coatings of graphene resulted in formation of irregular, tall, and porous morphologies due to disorder arrangement of the graphene layers and the pores or the open spaces between the tall structures held the working fluid that contributed toward the microlayer evaporation and liquid resupply mechanisms underlying enhanced boiling performance. We further confirmed the long-term sustainability on microscale coatings by conducting multiple boiling tests that drastically improved heat transfer coefficient. This resulted from the transition of superhydrophilic to superhydrophobic coatings supported by Fourier transform infrared, (FTIR) studies that confirmed the removal of hydroxyl-based functional groups from the surfaces (Rishi et al., 2019a; Rishi et al., 2019b).

Our preliminary investigation using graphene nanoplatelets (GNPs) based surface coatings produced record-breaking pool boiling performance with a very high critical heat flux at low wall superheat reported in the literature for graphene-based coatings on plain copper surfaces. This is attributed to their unique layered structure comprising tightly packed graphene sheets that render higher wettability than graphene sheets (Rishi et al., 2019a). This comprehensive study focused on copper and GNP-based composite coatings formed by combining various powder metallurgy and manufacturing techniques with a goal of creating tunable interconnect porous surfaces. Briefly, ball milling was used to combine copper and GNP powders which were then coated using sintering and salt-patterning techniques. The GNP and copper were also coated as is using electrodeposition. This paper provides the correlation between each coating method with their resultant surface morphologies and properties, and their consequences on the boiling enhancement mechanisms. These correlations can potentially be applied to the design of heat transfer equipment and devices.

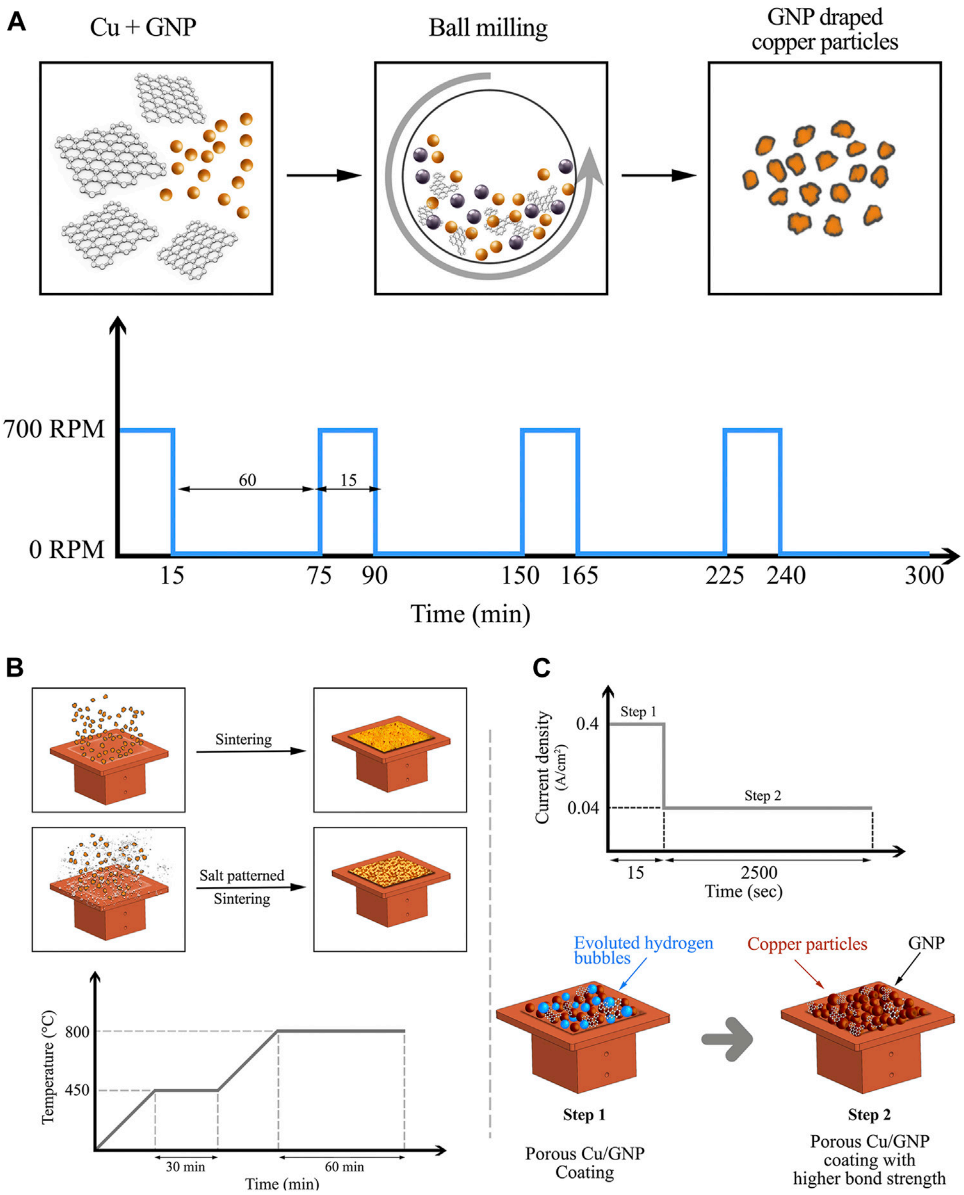

FIGURE 1 | (A) Schematic representation of the ball milling process, **(B)** Schematic illustration representing the sintering and salt-patterned sintering processes, and **(C)** plot showing two-step electrodeposition technique and schematic diagram representing the process of deposition.

MATERIALS AND METHODS: FORMATION OF COPPER/GRAPHENE NANOPLATELETS COMPOSITE POWDERS AND COATINGS

Graphene nanoplatelets (GNPs) with 500 m^2/g surface area were obtained from Alfa Aesar. Copper sulfate pentahydrate ($CuSO_4.5H_2O$) and conc. Sulfuric acid (H_2SO_4) required for electrodeposition were obtained from Fisher Scientific. Copper particles of 1, 20, 45, and 150 μm diameters were acquired from United States Research Nanomaterials Inc. Copper 101 used to fabricate test substrates was procured from McMaster Carr.

Copper/Graphene Nanoplatelets Composite Powder Formation via Ball Milling

A benchtop high-energy vibratory ball mill from Across International was used to create Cu/GNP-based composite powders. Stainless steel balls ~5 mm in diameter were used for milling. The mixture of GNP-copper particles along with ethanol as a process control agent was milled at 700 rpm for 1 h total with 1 h of resting period after every 15 min of milling. The resting period prevented the overheating and acted as a short annealing cycle which promoted GNP draping phase and alloying of GNP and copper, schematically as shown in **Figure 1A**.

Sintered and Salt Pattern-Based Coatings

The composite coatings were formed on plain copper test surfaces with an average surface roughness (Ra) of ~0.4 μm using electrodeposition and sintering techniques. Prior to coating, the test sections on the copper substrates were prepared to ensure the 1 cm^2 by covering the surplus area with Kapton tape. The exposed boiling area was thoroughly cleaned with distilled water and IPA. The ball-milled powders were mixed with urethane overprint clear screen binder obtained from Nazdar SourceOne and were screen printed on the plain copper test surfaces using a squeegee and a CP-100 frame. The binder to Cu/GNP powder weight ratio was kept constant at 1:2 for all the coatings. Screen-printed surfaces were then transferred to a sintering furnace and sintering was performed under inert helium atmosphere. The sintering process consisted of an initial heating with a ramp up to 450°C and the temperature was maintained constant for 30 min in order to burn off the binder from coating. This was followed by a second temperature ramp up to 800°C and holding at that temperature for 1 h. The sintered coatings (**Figure 1B**) were then allowed to cool down in the furnace to room temperature under continuous helium flow (Jaikumar et al., 2017c).

The salt-patterned samples were prepared by combining sodium carbonate pellets with screen printing binder and ball-milled Cu/GNP mixture. Salt pellets to ball-milled powder mixed at 1:3 ratio by weight was used to develop salt-patterned sintered coatings using the sintering parameters mentioned above. The process was concluded by immersing the coatings in distilled water for 30 min to eliminate salt pellets.

Electrodeposition-Based Coatings

A two-step electrodeposition method was developed to create Cu/GNP coatings with copper block as anode and copper test surface as cathode. The electrolyte consisted of copper sulfate, sulfuric acid, and distilled water. GNP was added to the electrolyte at 0.5, 1, 2, and 2.5 wt% concentrations. Further increase in the concentration of GNP led to the agglomeration and sedimentation of the GNP particles. A current density of 0.4 A/cm^2 was applied for 15 s ensuring the Cu/GNP deposition that resulted in the evolution of hydrogen gas bubbles due to the electrolysis of water in the electrolyte solution. This was followed by application of a lower current density of 0.04 A/cm^2 for 2,500 s as shown in **Figure 1C**. The lower current was insufficient to generate hydrogen bubbles and at this step, the existing hydrogen bubbles collapsed; thus, creating a hierarchical porous network on the surface (Patil and Kandlikar, 2014). The lower current step contributed in strengthening the bond between the particles that also resulted in their improved adhesion to the substrate. Electrodeposited coatings were generated with varying ratios of GNP by adding the calculated mass of GNP in the electrolyte.

Optical and Analytical Techniques for Surface Characterization of the Copper/Graphene Nanoplatelets Powders and Coatings

The surface morphology of electrodeposited and sintered coatings was observed using TESCAN Field Emission Mira III LMU and JEOL JSM-6400V scanning electron microscopes (SEM) operated at 15 kV. The elemental analysis of the composite coatings was performed using energy dispersive X-ray spectroscopy (EDS) measurements on Bruker Quantax EDS with XFLASH 5010 detector attached to a field emission SEM MIRA II LMH. Surface roughness of the coatings was analyzed by a scanning confocal laser microscope (Keyence VKX-200).

The combined morphologies of ball-milled copper and GNP powders were observed on Hitachi HD-2300 dual EDS scanning transmission electron microscope (STEM). FTS 4000-ATR Fourier transform infrared (FTIR) spectroscopy was performed on ball-milled copper/GNP powders to confirm the presence of graphene through observance of its functional groups. TA Instruments Q50 Thermogravimetric analyzer (TGA) was used to quantify the amount of GNP associated with copper particles as a result of ball milling by monitoring the weight change of the sample with increased temperature. Multi-wavelength Jobin Yvon Horriba Lab RAM HR Raman Spectroscopy using He-Ne Laser (λ = 632.8 nm) and Rigaku DMAZ-IIB X-Ray Diffractometer (XRD)(Cu Kα radiation and wavelength1.5418 Å) techniques were implemented for estimating the number of graphene layers and the quality of deposited graphene.

POOL BOILING TEST SETUP

A plain copper test surface and a heater block of copper (**Figure 2**) alloy 101 was manufactured using the CNC machine to measure the local temperature during boiling and heat supply, respectively. A schematic illustration of the entire pool boiling test setup used for all the experiments is presented in **Figure 2**. Four cartridge heaters (120 V-DC, 200 W each) were inserted into the sides of the copper heater block located at the bottom of the apparatus (**Figure 2**) and the 10 × 10 mm surface of the copper heater was kept in contact with the copper test surface, which also has a base section of 10 × 10 mm. This enabled 1-D heat conduction from the copper heater to the test surface. In order to minimize the thermal resistance between two mating surfaces (copper heater block and copper test surface), a grafoil sheet was placed (**Supplementary Figure S1**). Heat losses were minimized by an outside ceramic insulator. A National Instruments cDaq-9172 data acquisition system with an NI-9211 thermocouple input module was used to record the temperatures during testing, using K-type thermocouples. These temperatures values were then used to calculate the heat flux and heat transfer coefficients. A LabVIEW interface was used which displayed real time temperature value plot with respect to time and was employed for determining the critical heat flux (CHF) condition as temperature values shoot up very high at the CHF condition (Jaikumar et al., 2017a).

A garolite plate that was used as a support for the ceramic test surface holder is shown in **Figure 2**. On top of the copper test surface is a quartz glass water bath. Another plate was used to further support the water bath with reservoir. Rubber gaskets between the plates ensured a leak proof setup. A top aluminum

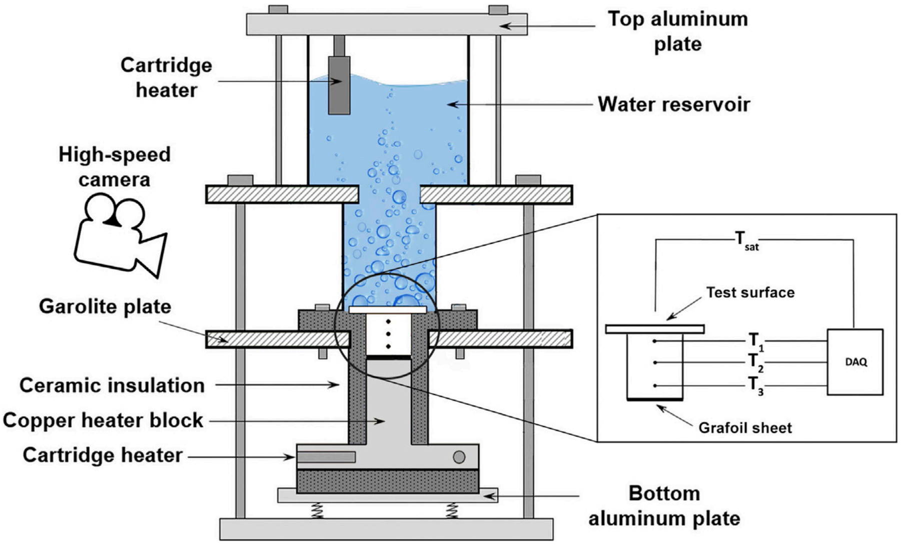

FIGURE 2 | Schematic representation of pool boiling apparatus.

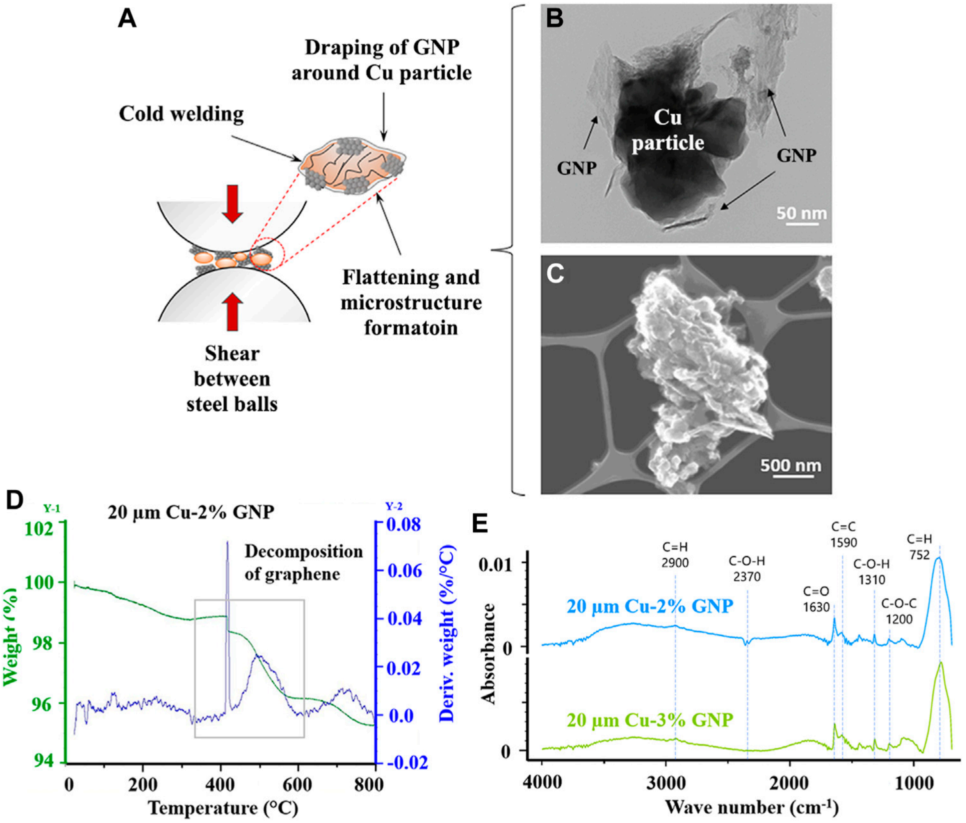

FIGURE 3 | (A) Schematic illustration representing the GNP draping mechanism during ball milling, **(B)** TEM image validating GNP draping around a copper particle (20 µm Cu-5% GNP), **(C)** STEM image depicting the morphological characteristics of GNP-draped-copper particle post ball milling (20 µm Cu-5% GNP), **(D)** Thermogravimetric analysis TGA showing variation in weight loss with increase in temperature (20 µm Cu-2% GNP), **(E)** Fourier transform infrared (FTIR) spectroscopy for ball milled and sintered coatings.

TABLE 1 | Fourier transform infrared spectra for GNP-based functional surfaces showing functional groups and corresponding absorption frequency regions.

Functional group	Absorption frequency	Description
C=C	1,590	Stretch-aromatic structure
C=H	752	Bend-alkenes, aromatic
	2,900	Stretch-alkanes, aldehydes
C-O-H	1,310	Stretch-alcohol
	2,350	Stretch-aldehyde
C=O	1,630	Stretch-ketones
C-O-C	1,200	Stretch-ester

plate was held at 60 V DC, 200 W auxiliary cartridge heater so that the water bath temperature could maintain boiling, continuously. Temperature was also monitored from the top via a thermocouple which is not shown in the schematic representation. The heat flux and heat transfer coefficients were calculated from collected temperature data (**Supplementary Figure S1**). All the pool boiling tests were performed with distilled water at an atmospheric pressure and the open loop system was used without using any condenser.

RESULTS AND DISCUSSIONS

Effects of Ball Milling on Copper/Graphene Nanoplatelets Compositing

Ball milling of copper particles of different diameters along with varying concentrations of GNP particles were performed that produced flattened composite particles. These composite particles undergo cold welding, plastic deformation, and work-hardening due to the shear forces arising from their entrapment between the colliding balls shown schematically in **Figure 3A**. As the copper particles work-harden, their microstructures are altered due to cyclic dynamic recovery and recrystallization. These collisions also increase the surface-to-volume ratio of the particles and the draping of GNP around copper particles. The ball milling cycle also included a short annealing cycle of 1 h after every 15 min of ball milling for cold welding of the copper and GNP particles that promotes the draping of GNP around copper particles as seen on **Figure 3B**. The images also confirm a drastic reduction in copper particle sizes from 20 μm to a few hundred nanometers post ball milling. STEM image of 20 μm Cu with 5 wt% GNP particles presented in **Figure 3C** reveals growth in surface roughness. Such microstructure alterations due to the processing methods also induce chemical and structural inhomogeneities that are highly desirable in pool boiling applications (Rishi et al., 2019a).

Thermogravimetric analysis (TGA) shown in **Figure 3D** further confirmed the presence of graphene as a sharp peak between 400 and 600°C that corresponds to the degradation of unstable carbon constituent of graphene (Gupta et al., 2018a). This also confirms the chemical and thermal stability of graphene nanoplatelets in Cu/GNP coatings during pool boiling experiments which were performed between 100 and 160°C.

Fourier transform infrared (FTIR) analysis also supported the association of GNP with copper particles through representation characteristic peaks of GNP functional groups. **Figure 3E** illustrates the FTIR spectra for 2 and 3 wt% of Cu/GNP coatings. The peaks include aromatic rings (C=C) at 1,570 cm^{-1}, stretching vibration C=O of carboxyl groups at 1,630 cm^{-1}, O–H deformation vibrations resulting from C–OH at 1,310 cm^{-1}, and C–O–C stretching vibration at 1,200 cm^{-1}. A summary of the peaks, their corresponding frequency region, and their structural description is provided in **Table 1**.

Coating Methods and Effects on Surface Morphology

One of the goals of this work was to investigate the efficacy of ball milling of copper and GNP particles prior to coating. In this regard, the study focused on comparing surfaces made by 1) electrodeposition of copper and GNP that were not ball milled, 2) sintering of ball milled particles, 3) adding salt-patterning step while sintering of ball-milled particles. **Figure 4** represents the laser optical images of 1) electrodeposited coatings, 2) sintered coating of ball-milled particles and, 3) sintered and salt-patterned coating of ball-milled particles along with their corresponding 3D surface analysis. The samples shown in **Figure 4** are chosen based on their highest pool boiling performance within each coating technique. All coatings in the figure have GNP additions and are imaged at the same magnification. The surface roughness (S_a) and maximum peak to valley measurements (S_z) indicated on the 3D mapping images were calculated using ISO 25178 code for surface texture analysis. No trends in these measurements could be discerned. However, close observation of the 3D images reveals highest level of surface porosity in the ball milling + salt-patterned + sintered coating. This is attributed to the additional salt-patterning step that allows for the formation of larger open pores nearly the size of salt pellets used for patterning.

3D-surface analysis performed by laser confocal microscope was complemented by electron microscopy to gain an insight on the interconnected porosity for the best pool boiling performing coatings 1) electrodeposited, 2) ball milled + sintered, and 3) ball milled + salt patterned + sintered. **Figure 5**A demonstrates taller hierarchical porous structures corresponding to the large peak to valley (Sz) possessed by the 2% GNP electrodeposited coatings. In contrast, **Figures 5B,C** showed reduced interconnected pores which is attributed to the flattening of the particles due to ball milling and spreading of the GNP sheets over flattened copper particles. The laser microscope confirms this, both ball-milled coatings have 50% or less Sz as compared to the 2% GNP electrodeposited coatings. The addition and subsequent removal of salt pellets after salt patterned sintering yielded deep, hollow, and highly variable in dimension-based structures analogous to the size of salt pellets in the range 40–200 μm. The higher depth and density of surface pores was also confirmed by 3D surface analysis (**Figure 4C**). In combination with ball milling, the salt-patterned resultant composite surfaces demonstrated greater and deeper surface porosity, which can be attributed to the flattening of the particles and spreading of the graphene sheets on the substrate.

ImageJ analysis was performed on all the SEM images to obtain correlation between equivalent projected circle (EQPC)

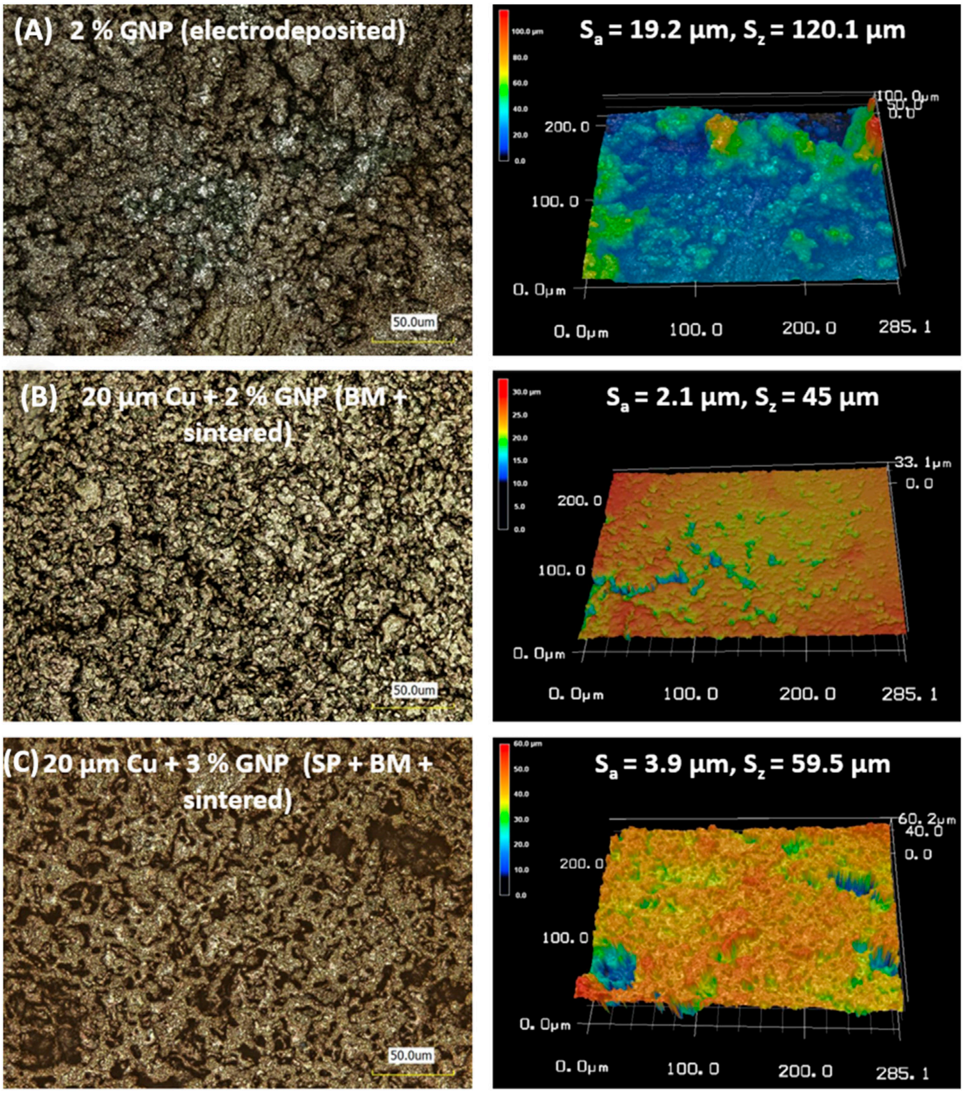

FIGURE 4 | Laser optical images for electrodeposited and sintered coatings representing S_a (surface roughness) and S_z (maximum peak to valley measurement) values and their corresponding 3D mapping images.

diameter of pores with number of pores as shown in **Figure 5D** (procedure provided in **Supplementary Section S3**). EQPC is a widely used method to estimate the projected area of the particles of arbitrary shapes; in this work, it was also used to assess the pore diameter (Hamilton et al., 2012; Li and Iskander, 2019). The plot on **Figure 5D** corresponds to the ImageJ analysis of the SEM images on **Figures 5A–C**. Ball-milled, sintered, and salt-templated coatings comprising of 20 µm diameter copper particles with 3 wt% GNP yielded maximum number of pores for almost all EQPC diameters ranging from 5 to 16 µm. Additional SEM images revealed larger pores (>50 µm) were also observed for salt-patterned sintered coatings. Wettability of the coatings was also investigated by measuring the static and dynamic contact angles. All GNP-based coatings, irrespective of their deposition technique, exhibited superhydrophilicity with a measure static and dynamic contact angles at 0°. Superior wetting and wicking properties of the coatings were imparted by the addition of GNP (**Supplementary Section S5**).

It was critical to investigate the impact of processing parameters on the native characteristics of the materials, and therefore Raman spectroscopy and XRD analysis were performed on the Cu/GNP coatings. **Figure 6A** presents Raman spectra with discrete G, D, and 2D graphene peaks at ~1,580, ~1,340, and ~2,700 cm^{-1}, respectively, for all GNP-based coatings. The G and D peaks correlate with the in-plane vibration of sp^2 hybridized carbon atoms and degree of disorder of sp^3 hybridized carbon structure, respectively (Childres et al., 2013). A small additional D’ peak observed at 1,610 cm^{-1} for all the deposited coatings irrespective of the method of deposition has been shown in an enlarged section. Ratio of G and 2D peak intensities (I_G/I_{2D}) define the number of deposited graphene layers, whereas the defects and damage

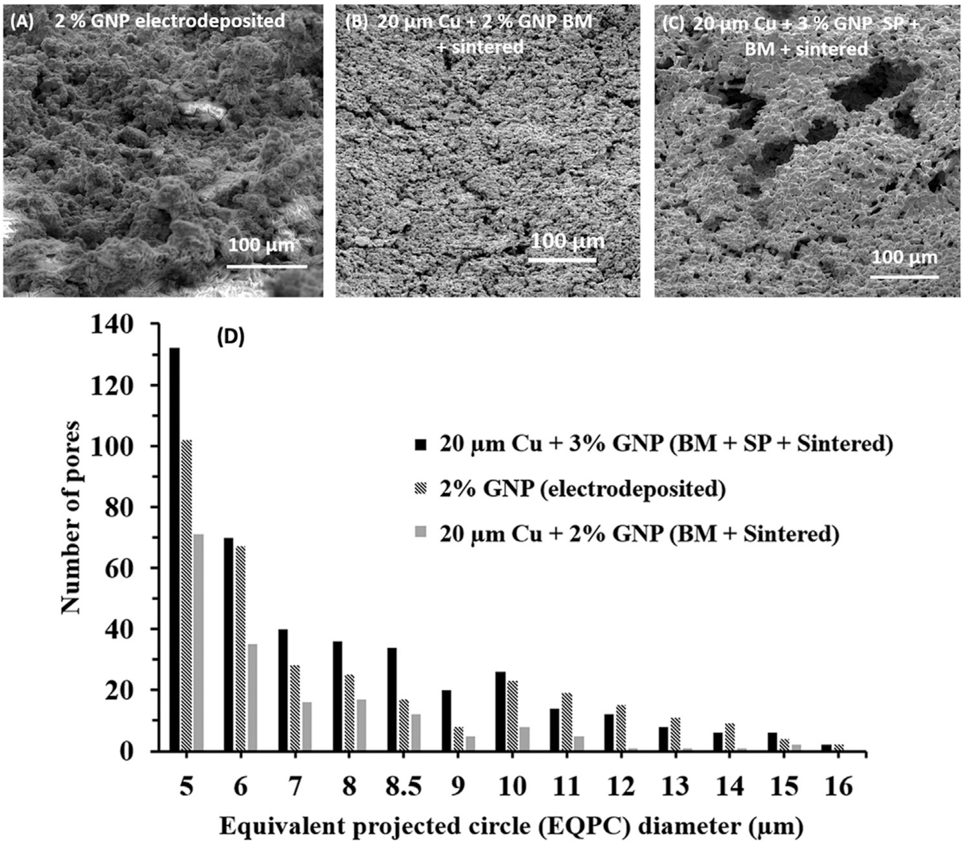

FIGURE 5 | 55° stage tilted scanning electron microscope images for **(A)** 2% GNP electrodeposited surface, **(B)** 20 µm Cu-2% GNP ball milled + sintered surface, and **(C)** 20 µm Cu-3% GNP ball milled + salt patterned sintered surface, **(D)** Plot showing the number of pores vs equivalent projected circle (EQPC) diameter of pores for different functional surfaces.

of graphene sheets are determined via ratios of D and G peak intensities (I_D/I_G) (Palaniselvam et al., 2012). In case of electrodeposited coatings, there was a linear increment in the number of deposited graphene layers corresponding to the increased GNP concentration until 2% GNP, and further increase in GNP resulted in poor electrodeposition due to the agglomeration of excess GNP in the electrolyte. A maximum of five layers were deposited for 2% GNP coating. In case of ball-milled and salt-patterned sintered coatings, the increase in GNP concentration caused the number of deposited graphene layers to grow with a maximum of ~6 layers for 20 µm Cu-3% GNP, and ~4 layers for 20 µm Cu-2% GNP, respectively. For all the coatings, I_D/I_G ratio was found to be less than one implying lesser defects and superior quality of deposited graphene (Rishi and Gupta, 2020).

X-ray diffraction (XRD) spectra on **Figure 6B** further confirmed no change in fundamental characteristics of both copper and GNP. As observed, the 2θ reflection peaks between 6–10°, and 20° correspond to graphene (G) and 47 and 54° are of copper. A broad and narrow reflection 2θ peak was observed for electrodeposited coating in the range of 6–10° compared to the peaks obtained for sintered coatings. This is attributed to lower concentration of GNP that was associated with copper particles due to their dilution in electrolyte, in contrast to ball milling, wherein larger amounts of GNP were able to associate with copper particles. This higher association of GNP with copper particles due to ball milling was confirmed by a broader diffracted graphene peak that was observed 20° implying a higher degree of disordered packing of larger number of graphene nanoplatelet layers (Blanton and Majumdar, 2013; Gupta et al., 2018b).

Enhanced Boiling Performance with Respect to Surface Characteristics

Pool boiling tests performed with water as the working fluid demonstrated higher heat transfer performance for electrodeposition and sintered coatings than that of nanoscale and homogeneous coatings. The tests were conducted until the CHF was reached, and the maximum heat transfer coefficient (HTC) was calculated by dividing critical heat flux with the wall superheat. The control tests with the plain copper surface yielded a CHF of 125 W/cm^2 and an HTC of 53 kW/m^2-°C. **Figures 7A,B** show the typical pool boiling curve and the calculated heat transfer coefficient vs. heat flux plots for the surfaces shown in **Figures 4**, **5**. Compared to a plain copper surface, all GNP-based

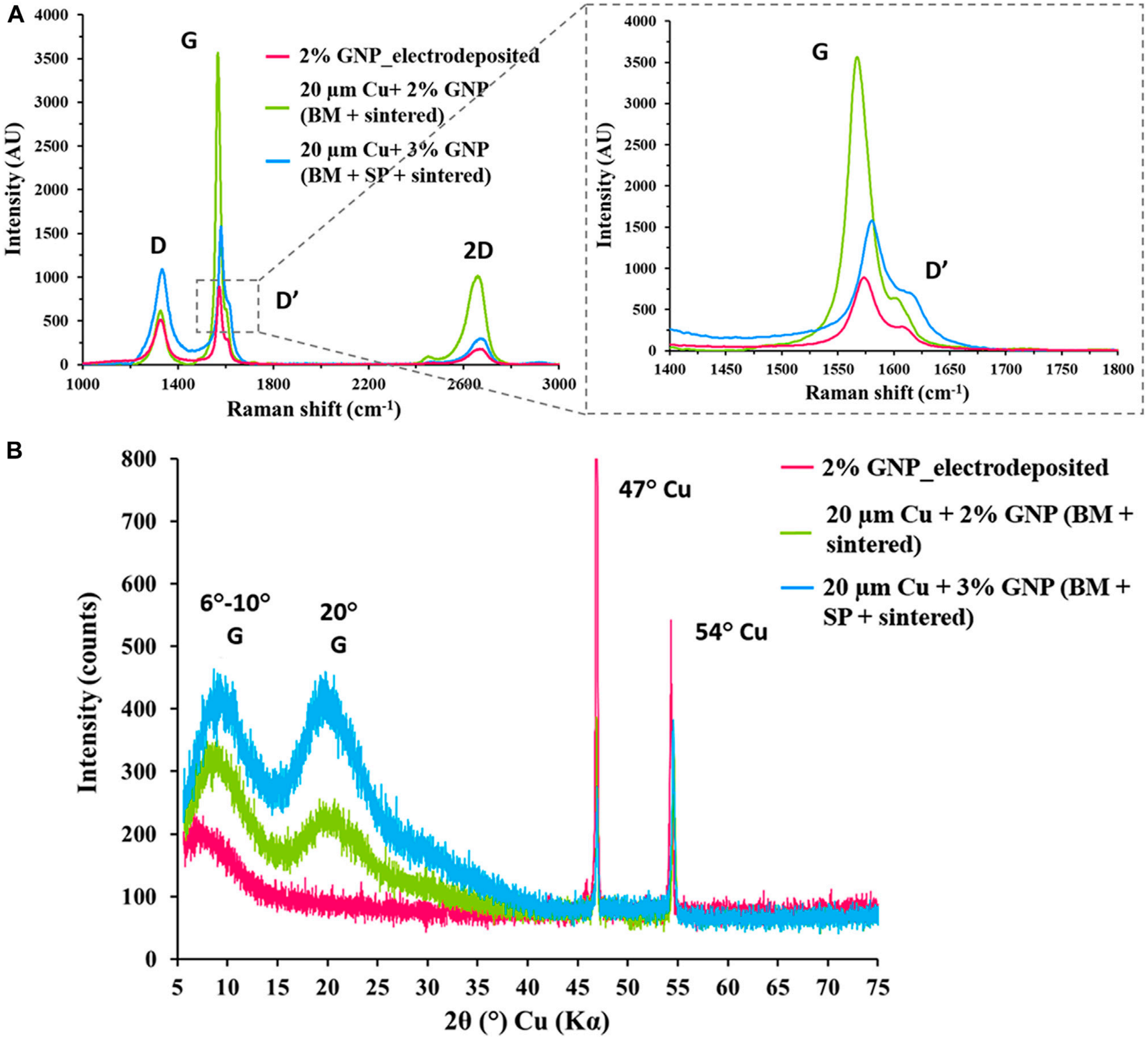

FIGURE 6 | (A) Raman spectroscopy analysis for 2% GNP electrodeposited surface and ball-milled sintered and salt-patterned sintered surfaces (2 and 3% GNP), 55° stage tilted scanning electron microscope images for **(B)** X-ray diffraction plot for electrodeposited and sintered surfaces.

functional surfaces demonstrated a drastic enhancement in terms of both CHF and HTC. For electrodeposited surface with 2 wt% GNP, the CHF and HTC of 286 W/cm^2 and 204 kW/m^2-°C was attained. Whereas the CHF and HTC for 20 µm Cu-2% GNP ball-milled and sintered (BM + sintered) coating was 239 W/cm^2 and 285 kW/m^2-°C. The maximum improvement in both CHF and HTC was obtained for 20 µm Cu-3% GNP ball-milled- and salt-pattern-based sintered (BM + SP + sintered) coating, with a CHF of 289 W/cm^2 and HTC of 1,314 kW/m^2-°C.

Typically, during pool boiling, wall superheat temperature of the heater surface increases with increment in heat flux until CHF. However, in this work, interestingly, for all GNP-based functional surfaces, irrespective of their coating techniques, a unique phenomenon of reduction in wall superheat temperature with increment in heat flux was observed. This phenomenon is termed as “boiling inversion” by researchers. For 2% GNP electrodeposited surface, boiling inversion was observed when heat flux was increased from 70 to 93 W/cm^2 and from 201 to 221 W/cm^2, whereas for 20 µm Cu-2% GNP ball-milled and sintered (BM + sintered) coating was from 43 to 64 W/cm^2. In case of 20 µm Cu-3% GNP ball-milled- and salt-pattern-based sintered (BM + SP + sintered) coating, boiling inversion was observed during the step increment of heat flux from 129 to 159 W/cm^2. It is postulated that the effect of active nucleation sites is maximized at these heat fluxes which causes the intensified bubble activity on the heater surface leading to a drastic reduction in the wall superheat temperature with an increment in heat flux. Boiling inversion is an intricate phenomenon and in the case of

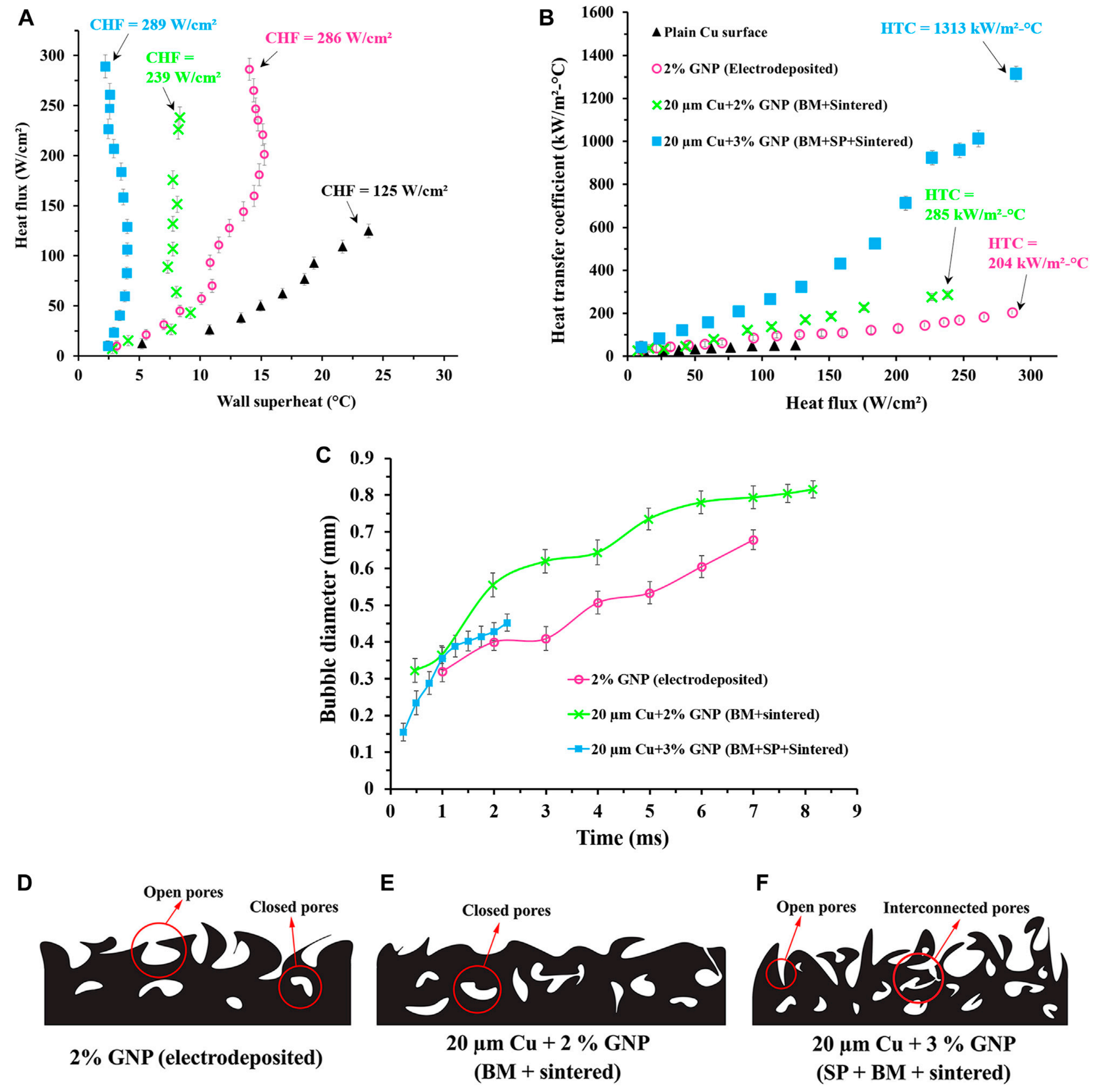

FIGURE 7 | (A) Pool boiling plot showing the variation of heat flux with respect to temperature and, **(B)** Heat transfer coefficients of GNP-based functional surfaces developed using electrodeposition, ball milling followed by sintering (BM + sintered), and ball milling followed by salt patterned sintering (BM + SP + sintered), **(C)** Plot indicating the bubble diameter propagation with time, schematic representing the types of pores formed for **(D)** 2% GNP electrodeposited surface, **(E)** 20 μm Cu-2% GNP ball milled + sintered surface, and **(F)** 20 μm Cu-3% GNP ball-milled + salt-patterned sintered surface.

GNP-based functional surfaces, this inversion is attributed to various factors including formation of hierarchical pores, efficient liquid supply pathways, interconnected pore formation, deposition of GNP layers, and active nucleation site density.

These high CHF and HTC obtained for the coatings can be correlated to their unique surface morphologies. The higher CHF of 286 W/cm^2 obtained for the electrodeposited coating is due to the presence of the tall ridge like structures as observed in **Figure 5A**. The void spaces between the taller structures supply a liquid reservoir that induces microlayer evaporation. The microlayer enhances the nucleation on the surface and subsequently, increases the heat flux dissipation. Additionally, these types of structures create roughness by increasing wickability at the submicron scale. However, when compared to ball-milled surfaces, the HTC obtained for electrodeposited surfaces were observed to be lower at ~204 kW/m^2-°C. The CHF obtained for ball-milled and sintered coating was found to be 239 W/cm^2 which is comparatively lower than CHF obtained for electrodeposited coatings. This is ascribed to the flatness of the GNP-copper particles induced by their collisions with balls and walls of mill, and the subsequent spreading or draping of GNP on copper that occurs during the ball milling as seen in **Figure 5B**. This flatter surface lacked optimum roughness to induce microlayer evaporation to enhance heat dissipation through bubble nucleation. However, a higher HTC was obtained for this coating than that of electrodeposited coatings. An extensive electron microscopy investigation indicated the presence of open and closed pores on these coatings (provided in **Supplementary Section S4**) which is responsible for a higher HTC by the means of efficient liquid supply pathways. SEM image analysis mentioned in the **Supplementary Section S4**, shows both top view and stage titled views of the morphology and indicates the additional liquid supply pathways for BM + sintered and BM + SP + sintered coatings. Electrodeposited coatings possessed open pores as shown schematically in **Figure 7D** that yielded pathways for bubble departure to improve the critical heat flux but could not provide efficient liquid supply to nucleation sites, leading to the reduction in the HTC compared to ball-milled and sintered coating. As again, the schematics in **Figures 7E,F** indicate the formation of open, closed, and interconnected pores, making them efficient for liquid supply, and thus improving the HTC.

The reduced heat dissipation or lower CHF obtained with sintered coating comprising of ball-milled particles was overcome by implementing a salt-patterning step that formed interconnected porous network and provided larger liquid retention sites for enabling microlayer evaporation. These larger pores also delayed horizontal bubble coalescence (Jaikumar and Kandlikar, 2016; Rishi et al., 2020a) and effectively cooled the heater surface by providing the highest heat transfer coefficient of 1,314 kW/m^2-°C achieved till date for porous coatings on plain copper surfaces. Such variation in pore dimensions obtained via salt-patterning also provides secondary boiling effects which are also established in literature (Kruse et al., 2016). In terms of pore characteristics discussed earlier, the pores resulting from ball-milled particles and more so, salt-patterning, demonstrated maximum number of pores (**Figure 5D**) and closed pore morphology schematically illustrated in **Figure 7F**. It is hypothesized that these closed pores introduced a large thermal gradient during boiling, which primarily reduced the wall superheat temperature, thereby increasing the HTC as observed in **Figure 7A**. Further investigations regrading individual effects of deposited GNP layers and their effects on morphology of the coating are being conducted.

High-speed image analysis was also performed on GNP-based functional surfaces to investigate the enhancement mechanism responsible for such dramatic improvements in overall pool boiling performance. Ideally, a smaller vapor bubble with lower departure time is expected for efficient heat transfer. Bubble departure diameters were measured for different surfaces by capturing high-speed videos using Photron Fastcam high-speed camera at 2,000 fps and a heat flux of ~15 W/cm^2. After performing a baseline study, plain copper surface attained the bubble departure diameter of 2.1 mm with a departure time of 13.25 ms. Bubble departure diameters for three surfaces, 2% GNP electrodeposited, 20 μm Cu-2% GNP ball milled + sintered, and 20 μm Cu-3% GNP ball milled + salt patterned sintered were also measured. Because of maximum CHF and HTC, the 20 μm Cu-3% GNP ball milled + salt patterned sintered surface exhibited the lowest bubble departure diameter of 0.45 mm with a departure time of only 2.25 ms. As opposed to that, bubble departure diameter and departure time for 2% GNP electrodeposited surface and 20 μm Cu-2% GNP ball milled + sintered surface were 0.68 mm, 7 ms, 0.81 mm, and 8 ms, respectively. **Figure 7C** shows the comparison of vapor bubble progression and departure diameters for different surfaces. These values are plotted with respect to time. Time was calculated by considering the total record time and corresponding frames per seconds at which the video was captured (2,000 fps). The shortest bubble departure diameter and time for 20 μm Cu-3% GNP ball milled + salt patterned sintered surface was also regarded as the significant factors in achieving a record-breaking CHF and HTC values.

In addition to bubble departure diameter and time, bubble release frequency is also one of the important parameters that dictate the overall pool boiling performance. One of the most comprehensive correlations between bubble release frequency and vapor bubble departure diameter is provided by Malenkov (1971). Based on this, a bubble release frequency was estimated for all the three coatings used in this study with the following equation:

$$fD_d = \frac{V_d}{\pi^*\left(1 - \frac{1}{1 + V_d * \rho_v * h_{fg} / q}\right)}, \tag{1}$$

where, f is the bubble release frequency (numbers/second), D_d is the vapor bubble departure diameter (m), ρ_l and ρ_v are densities of liquid and vapor (kg/m³), g is the acceleration due to gravity (m/s^2), σ is the surface tension of the liquid at saturation conditions (N/m), h_{fg} is the latent heat of vaporization (J/kg), q is the corresponding heat flux (W/m^2), and V_d represents the velocity of the departing bubble (m/s). Here, V_d is given by **Eq. 2** (Dhir, 2018).

$$V_d = \sqrt{\frac{D_d * g * (\rho_I - \rho_v)}{2 * (\rho_I + \rho_v)} + \frac{2 * \sigma}{D_d * (\rho_I + \rho_v)}}. \tag{2}$$

During boiling, a new bubble can grow only when the pressure at the nucleation cavity becomes equal to the total pressure at the heated surface. With increase in heat flux, bubble release frequency from nucleation sites increase and bubbles merge in the vertical direction forming vapor columns (Dhir, 2018). A smaller bubble diameter and departure time, and a higher bubble release frequency, thus, provides a rapid heat transfer allowing greater reduction in the wall superheat temperature. Based on the measured vapor bubble departure diameters for each of the coating, bubble release frequency was calculated. A maximum bubble release frequency f of approximately 450 was obtained for 20 μm Cu-3% GNP ball milled + salt patterned sintered surface,

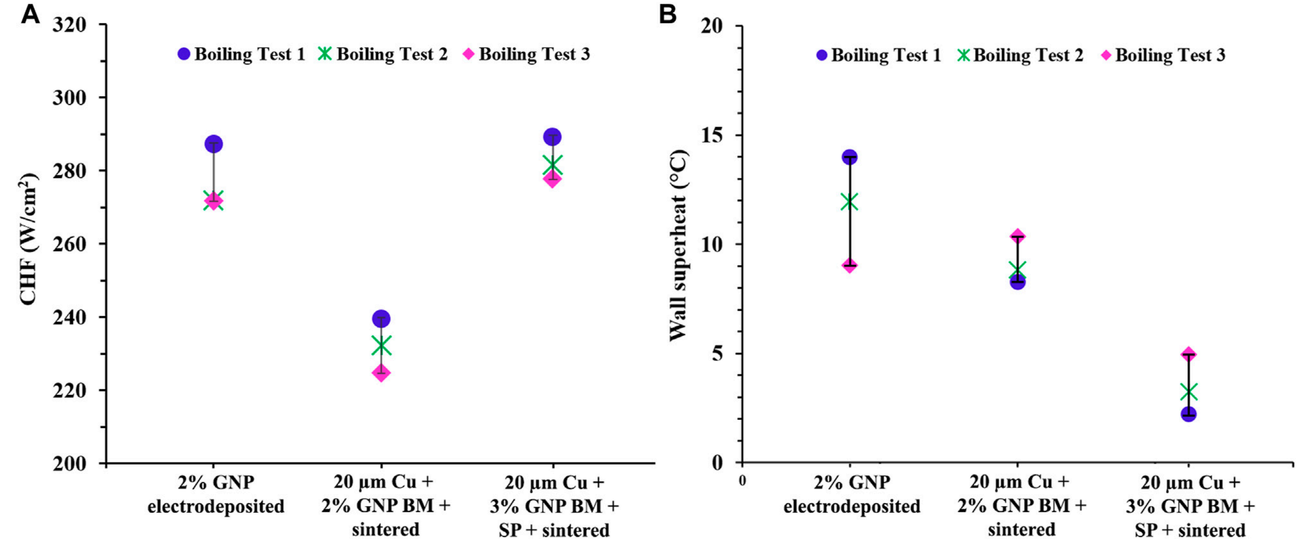

FIGURE 8 | (A) Plot comparing the CHF values, and **(B)** wall superheat values of repetitive boiling tests for 2% GNP electrodeposited surface, 20 µm Cu-2% GNP BM (ball milled) + sintered surface, and 20 µm Cu-3% GNP BM + salt patterned (SP) sintered surface.

around 250 for 2% GNP electrodeposited surface, and 210 for 20 µm Cu-2% GNP ball milled + sintered surface. This value depicts extremely large number of vapor bubble release from the heated surface, and thus contributed in achieving the highest HTC for the salt-patterned surface. At higher heat fluxes, owing to high heat input, bubble release frequency increases further and the activation of additional nucleation sites contribute in obtaining higher heat transfer coefficients.

Pool Boiling Durability Studies of Graphene Nanoplatelets-Based Functional Surfaces

Pool boiling is an extremely vigorous process and a continuous vapor bubble activity on the heater surface during boiling can deteriorate the boiling performance and peel-off the coating. Thus, to test the efficacy and sustainability of the coatings for repetitive pool boiling testing, three repetitive boiling tests were conducted until the CHF condition for the best performing composition, that is, for 2% GNP electrodeposited surface, 20 µm Cu-2% GNP BM + sintered surface, and 20 µm Cu-3% GNP BM + salt-patterned sintered surface. **Figures 8A,B** shows the CHF and wall superheat value ranges for three repetitive tests. Interestingly, with repetitive testing, the wall superheat temperature for 2% GNP electrodeposited coating was reduced, indicating a higher heat transfer coefficient. In our previous work, we have performed a detailed study on these electrodeposited surfaces and we concluded that owing to reduction of GNP to r-GNP, the reduction in wall superheat temperature is achieved. Reduced-GNP (r-GNP) is the reduced form of GNP which has less oxygen and hydroxyl groups than GNP and possesses higher thermal properties (Rishi et al., 2020b).

It was observed that repetitive testing for these three surfaces did not show a significant deterioration in heat transfer performance of the coatings, indicating the strong adhesion and cohesion of the deposited GNP/Cu material with the base copper heater surface. Nonetheless, future in-depth studies are warranted for these coatings with primary focus on observation of the effect of additional repetitive boiling tests on overall morphology of the coatings and their effect on overall pool boiling performance. The strong adhesion and cohesion obtained for the coatings used in this study is attributed to the addition of GNP and formation of strong bonds using electrodeposition and sintering based techniques.

Both electrodeposition and sintering techniques have a huge potential for large scale applications with moderate costs of coating preparation. Unlike sintering, electrodeposition technique does not require high temperature furnace and longer duration, and thus will be more cost-effective than sintering technique. Electrodeposition technique can be used for the surface of any size and shape and comparatively requires less time to create coatings than sintering technique. In case of sintering, a multiple number of heater surfaces can be sintered at a time in a sintering furnace, making it suitable for large scale applications. However, a thorough analysis on the effect of repetitive testing on coatings and on CHF and HTC is essential before applying these techniques to large scale applications.

This paper presents a detailed discussion on various simple and cost-effective coating processes, their resultant morphologies and surface properties such as wettability, porosity, and roughness that have demonstrated to improve the boiling performance, also summarized in **Table 2**. It is postulated that the pool boiling enhancement of these surfaces is due to the combination of various factors such as the formation of unique microporous structure, copper/GNP composite deposition, number of deposited graphene layers, increased wicking properties, and bubble dynamics on the heater surface.

TABLE 2 | Common and distinguishing factors responsible for enhancements in pool boiling performance for GNP-based functional surfaces.

Process coating technique	Characteristics of coated functional surfaces	Enhancement mechanisms (distinguishing factors)
2% GNP_electrodeposited	• Hierarchical porous coating with wide range (0.5–20 μm) of porosity	• Taller morphological structure with more open pores—promoted microlayer evaporation
	• XRD—smaller peaks with less disordering	• Higher CHF and HTC (286 W/cm^2, HTC-204 kW/m^2-°C respectively)
20 μm Cu-2% GNP (BM + sintered)	• Flatter porous coating with rectangular shape pores	• Flatter structures due to ball milling and sintering. • Efficient liquid supply to nucleation sites owing to distinguished coating formation
	• XRD—broader peaks, additional 20° peak indicating disordered structure with more carbon	• Higher HTC (285 kW/m^2-°C), CHF-(239 W/cm^2)
20 μm Cu-3% GNP (BM + SP + sintered)	• Highly variable ranged (1.5–200 μm) porous structure with tunnels	• Tall microstructures, closed pores–high thermal gradient. • Tunnels and interconnected porous coating—highly efficient liquid supply to nucleation sites
	• XRD—broader and higher peaks, additional 20° peak indicating disordered structure with more carbon	• Highest CHF and HTC (289 W/cm^2, 1,314 kW/m^2-°C)

CONCLUSION

In this work, we present various copper/graphene nanoplatelets (Cu/GNP) based composite coatings for their applications in pool boiling heat transfer. This work focused on drawing the correlations between the coating methods, the effects of process steps on surface morphology that gives rise to superior properties, particularly, wickability, wettability, porosity, and roughness that govern the boiling performance. It was established that coating processes can be tuned to create surfaces with hierarchical interconnected pores that contribute in microlayer evaporation for higher hear dissipation. Electrodeposition processes rendered taller structures with void spaces between them that acted as liquid retention as well as nucleation sites and, this was responsible for a very critical heat flux. Sintering coating was also investigated to overcome the agglomeration of higher concentration of GNP in the electrolyte during electrodeposition. A preliminary step of ball milling of copper and GNP before sintered coating was introduced that led to flatter surfaces with additional roughness. Additionally, salt-patterning was implemented with sintering to control the pore sizes analogous to the sizes of the salt pellets. Sintered coatings with salt-patterning produced record-breaking heat transfer coefficients of 1,314 kW/m^2-°C which is attributed to efficient vapor removal and the thermal gradient formations inside the interconnected closed pores that reduced the wall superheat due to cooling effects. The proposed surface functional coatings can potentially be applied to heat transfer equipment or devices and high temperature electronics cooling applications.

DATA AVAILABILITY STATEMENT

The original contributions presented in the study are included in the article/**Supplementary Material**, further inquiries can be directed to the corresponding author.

AUTHOR CONTRIBUTIONS

All the authors contributed to the manuscript contributed equally. All authors contributed to manuscript revision, read, and approved the submitted version.

FUNDING

The authors gratefully acknowledge the financial support provided by the American Chemical Society Petroleum Research Fund for this research.

SUPPLEMENTARY MATERIAL

The Supplementary Material for this article can be found online at: https://www.frontiersin.org/articles/10.3389/fmech.2021.642214/full#supplementary-material.

REFERENCES

Amalfi, R. L., Cataldo, F., Marcinichen, J. B., and Thome, J. R. (2020). “Experimental characterization of a server-level thermosyphon for high-heat flux dissipations,” in 2020 19th IEEE intersociety conference on thermal and thermomechanical phenomena in electronic systems (ITherm), Orlando, FL, July 21–23 2020 (New York, NY: IEEE), doi:10.1109/ITherm45881.2020.9190186

Antonelli, R., and O’Neill, P. S. (1981). “Design and application considerations for heat exchangers with enhanced boiling surfaces,” in Advanced Course in Heat Exchangers: Theory and Practice. ICHMT Symposium, Dubrovnik, Croatia, 1981 (New York, NY: Begel House Inc.). doi:10.1615/ICHMT.1981.AdvCourseHeatExch.140

Blanton, T. N., and Majumdar., D. (2013). Characterization of X-ray irradiated graphene oxide coatings using X-ray diffraction, X-ray photoelectron spectroscopy, and atomic force microscopy. *Powder Diffr.* 28 (2), 68–71. doi:10.1017/s0885715613000109

Cao, Z., Liu, B., Preger, C., Wu, Z., Zhang, Y., Wang, X., et al. (2018). Pool boiling heat transfer of FC-72 on pin-fin silicon surfaces with nanoparticle deposition. *Int. J. Heat Mass Transfer* 126, 1019–1033. doi:10.1016/j.ijheatmasstransfer.2018.05.033

Chauhan, A., and Kandlikar, S. G. (2019). Characterization of a dual taper thermosiphon loop for CPU cooling in data centers. *Appl. Therm. Eng.* 146, 450–458. doi:10.1016/j.applthermaleng.2018.10.010

Childres, I., Jaureguib, L. A., Parkb, W., Caoa, H., and Chena, Y. P. (2013). *Raman Spectroscopy of Graphene and Related Materials*.

Cooke, D., and Kandlikar, S. G. (2012). Effect of open microchannel geometry on pool boiling enhancement. *Int. J. Heat Mass Transfer* 55 (4), 1004–1013. doi:10.1016/j.ijheatmasstransfer.2011.10.01

Dhir, V. K. (2018). "Nucleate pool boiling," in *Handbook of thermal Science and engineering*, Editor F. Kulacki (New York, NY: Springer). doi:10.1007/978-3-319-26695-4_41

Gajghate, S. S., Vashistha, S., Saha, B. B., and Bhaumik, S. (2020). Experimental and numerical investigation of pool boiling heat transfer over different thickness of graphene-poly(3,4-ethylenedioxythiophene):poly(styrenesulfonate) layers on copper heater surface. *Heat Transfer Eng.*, 1–20. doi:10.1080/01457632.2020.1777013

Gupta, A., Jaikumar, A., Kandlikar, S. G., Rishi, A., and Layman, A. (2018a). A multiscale morphological insight into graphene based coatings for pool boiling applications. *Heat Transfer Eng.* 39 (15), 1331–1343. doi:10.1080/01457632.2017.1366228

Hamilton, P., Littlejohn, D., Nordon, A., Sefcik, J., and Slavin, P. (2012). Validity of particle size analysis techniques for measurement of the attrition that occurs during vacuum agitated powder drying of needle-shaped particles. *Analyst* 137 (1), 118–125. doi:10.1039/c1an15836h

Jaikumar, A., Gupta, A., Kandlikar, S. G., Yang, C. Y., and Su, C. Y. (2017a). Scale effects of graphene and graphene oxide coatings on pool boiling enhancement mechanisms. *Int. J. Heat Mass Transfer* 109, 357–366. doi:10.1016/j.ijheatmasstransfer.2017.01.110

Jaikumar, A., Kandlikar, S. G., and Gupta, A. (2017b). Pool boiling enhancement through graphene and graphene oxide coatings. *Heat Transfer Eng.* 38 (14–15), 1274–1284. doi:10.1080/01457632.2016.1242959

Jaikumar, A., and Kandlikar, S. G. (2016). Pool boiling enhancement through bubble induced convective liquid flow in feeder microchannels. *Appl. Phys. Lett.* 110 (4), 094107. doi:10.1063/1.4941032

Jaikumar, A., Rishi, A., Gupta, A., and Kandlikar, S. G. (2017c). Microscale morphology effects of copper–graphene oxide coatings on pool boiling characteristics. *J. Heat Transfer* 139, 111509. doi:10.1115/1.4036695

Kandlikar, S. G. (2017). Enhanced macroconvection mechanism with separate liquid–vapor pathways to improve pool boiling performance. *J. Heat Transfer* 139, 051501. doi:10.1115/1.4035247

Kandlikar, S. G. (2013). Controlling bubble motion over heated surface through evaporation momentum force to enhance pool boiling heat transfer. *Appl. Phys. Lett.* 102 (5), 051611. doi:10.1063/1.4791682

Kandlikar, S. G. (2019). *Handbook of phase change: boiling and condensation*. London, United Kingdom: Routledge.

Kercher, D. S., Lee, J. B., Brand, O., Allen, M. G., and Glezer, A. (2003). Microjet cooling devices for thermal management of electronics. *IEEE Trans. Compon. Packaging Technol.* 26 (2), 359–366. doi:10.1109/tcapt.2003.815116

Kong, X., Zhang, Y., and Wei, J. (2018). Experimental study of pool boiling heat transfer on novel bistructured surfaces based on micro-pin-finned structure. *Exp. Therm. Fluid Sci.* 91, 9–19. doi:10.1016/j.expthermflusci.2017.09.021

Konishi, C., and Mudawar, I. (2015). Review of flow boiling and critical heat flux in microgravity. *Int. J. Heat Mass Transfer* 80, 469–493. doi:10.1016/j.ijheatmasstransfer.2014.09.017

Kruse, C., Tsubaki, A., Zuhlke, C., Anderson, T., Alexander, D., Gogos, G., et al. (2016). Secondary pool boiling effects. *Appl. Phys. Lett.* 108 (5), 051602. doi:10.1063/1.4941081

Lavrikov, A. V., Hammerschmidt, J., Kuzma-Kichta, Y. A., and Scholl, S. (2015). Thermosiphon reboilers with enhanced tubes. *Chem. Ing. Tech.* 87 (3), 290–296. doi:10.1002/cite.201400056

Lee, S., Seo, G. H., Lee, S., Jeong, U., Lee, S. J., Kim, S. J., et al. (2016). Layer-by-Layer carbon nanotube coatings for enhanced pool boiling heat transfer on metal surfaces. *Carbon* 107, 607–618. doi:10.1016/j.carbon.2016.06.039

Li, L., and Iskander, M. (2019). Evaluation of dynamic image analysis for characterizing granular soils. *Geotech. Test. J.* 43 (5), 1149–1173. doi:10.1520/gtj20190137

Malenkov, I. G. (1971). Detachment frequency as a function of size for vapor bubbles. *J. Eng. Phys.* 20 (6), 704–708. doi:10.1007/bf01122590

McLaughlin, C. (2019). Directional notches as microstructures to promote nucleation and heat transfer in pool boiling. Thesis. Rochester (NY): Rochester Institute of Technology.

Mudawar, I. (2017). Chapter five-flow boiling and flow condensation in reduced gravity. *Adv. Heat Transf.* 49, 225–306. doi:10.1016/bs.aiht.2017.06.002

Ohta, H., Ohno, T., Hioki, F., and Shinmoto, Y. (2004). Development of a high-performance boiling heat exchanger by improved liquid supply to narrow channels. *Ann. N. Y Acad. Sci.* 1027, 217–234. doi:10.1196/annals.1324.019

Orman, Ł. J., Radek, N., Pietraszek, J., and Gontarski, D. (2019). Phase change heat exchangers made of pin-fins for boiling enhancement. *Conf. Qual. Prod. Improvement* 1 (1), 433–439. doi:10.2478/9783110680591-059

Palaniselvam, T., Aiyappa, H. B., and Kurungot, S. (2012). An efficient oxygen reduction electrocatalyst from graphene by simultaneously generating pores and nitrogen doped active sites. *J. Mater. Chem.* 22 (45), 23799–23805. doi:10.1039/c2jm35128e

Park, S. D., Moon, S. B., and Bang, I. C. (2014). Effects of thickness of boiling-induced nanoparticle deposition on the saturation of critical heat flux enhancement. *Int. J. Heat Mass Transfer* 78, 506–514. doi:10.1016/j.ijheatmasstransfer.2014.06.090

Patil, C. M., and Kandlikar, S. G. (2014). Pool boiling enhancement through microporous coatings selectively electrodeposited on fin tops of open microchannels. *Int. J. Heat Mass Transfer* 79, 816–828. doi:10.1016/j.ijheatmasstransfer.2014.08.063

Patil, C. M., Santhanam, K. S. V., and Kandlikar, S. G. (2014). Development of a two-step electrodeposition process for enhancing pool boiling. *Int. J. Heat Mass Transfer* 79, 989–1001. doi:10.1016/j.ijheatmasstransfer.2014.08.062

Pi, G., Deng, D., Chen, L., Xu, X., and Zhao, C. (2020). Pool boiling performance of 3D-printed reentrant microchannels structures. *Int. J. Heat Mass Transfer* 156, 119920. doi:10.1016/j.ijheatmasstransfer.2020.119920

Raghupathi, P. A., and Kandlikar, S. G. (2017). Pool boiling enhancement through contact line augmentation. *Appl. Phys. Lett.* 110 (20), 204101. doi:10.1063/1.4983720

Rishi, A. M., Kandlikar, S. G., and Gupta, A. (2020a). Salt templated and graphene nanoplatelets draped copper (GNP-Draped-Cu) composites for dramatic improvements in pool boiling heat transfer. *Sci. Rep.* 10 (1), 11941. doi:10.1038/s41598-020-68672-1

Rishi, A. M., Gupta, A., and Kandlikar, S. G. (2018). Improving aging performance of electrodeposited copper coatings during pool boiling. *Appl. Therm. Eng.* 140, 406–414. doi:10.1016/j.applthermaleng.2018.05.061

Rishi, A. M., Kandlikar, S. G., and Gupta, A. (2019a). Improved wettability of graphene nanoplatelets (GNP)/Copper porous coatings for dramatic improvements in pool boiling heat transfer. *Int. J. Heat Mass Transfer* 132, 462–472. doi:10.1016/j.ijheatmasstransfer.2018.11.169

Rishi, A. M., Kandlikar, S. G., and Gupta, A. (2019b). Repetitive pool boiling runs: a controlled process to form reduced graphene oxide surfaces from graphene oxide with tunable surface chemistry and morphology. *Ind. Eng. Chem. Res.* 58 (17), 7156–7165. doi:10.1021/acs.iecr.8b06062

Rishi, A. M., Kandlikar, S. G., Rozati, S. A., and Gupta, A. (2020b). Effect of ball milled and sintered graphene nanoplatelets-copper composite coatings on bubble dynamics and pool boiling heat transfer. *Adv. Eng. Mater.* 22 (7), 1901562. doi:10.1002/adem.201901562

Rishi, A. M., and Gupta, A. (2020). "Fundamental insight on morphological changes of graphene nanoplatelets-copper (GNP-Cu) coatings: effects of repetitive pool boiling tests," in ASME 2020 18th International Conference on Nanochannels, Microchannels, and Minichannels collocated with the ASME 2020 Heat Transfer Summer Conference and the ASME 2020 Fluids Engineering Division Summer Meeting, Orlando, FL, July 13–15, 2020. doi:10.1115/ICNMM2020-1027

Sadaghiani, A. K., Saadi, N. S., Parapari, S. S., Karabacak, T., Keskinoz, M., and Koşar, A. (2017). Boiling heat transfer performance enhancement using micro and nano structured surfaces for high heat flux electronics cooling systems. *Appl. Therm. Eng.* 127, 484–498. doi:10.1016/j.applthermaleng.2017.08.018

Sinha-Ray, S., Zhang, W., Stoltz, B., Sahu, R. P., Sinha-Ray, S., and Yarin, A. L. (2017). Swing-like pool boiling on nano-textured surfaces for microgravity applications related to cooling of high-power microelectronics. *NPJ Microgravity* 3 (1), 1–9. doi:10.1038/s41526-017-0014-z

Thome, J. R. (1988). Reboilers with enhanced boiling tubes. *Heat Transfer Eng.* 9 (4), 45–62. doi:10.1080/01457638808939680

Vasudevan, D., Senthilkumar, D., and Surendhiran, S. (2020). Performance and characterization studies of reduced graphene oxides aqua nanofluids for a pool boiling surface. *Int. J. Thermophys.* 41 (6), 74. doi:10.1007/s10765-020-02651-6

Walunj, A., and Sathyabhama, A. (2018). Comparative study of pool boiling heat transfer from various microchannel geometries. *Appl. Therm. Eng.* 128, 672–683. doi:10.1016/j.applthermaleng.2017.08.157

Wei, J., Zhao, J., Yuan, M., and Xue, Y. (2009). Boiling heat transfer enhancement by using micro-pin-finned surface for electronics cooling. *Microgravity Sci. Tec.* 21 (1), 159–173. doi:10.1007/s12217-009-9137-5

Yao, Z., Lu, Y. W., and Kandlikar, S. G. (2012). Fabrication of nanowires on orthogonal surfaces of microchannels and their effect on pool boiling. *J. Micromech. Microeng.* 22, 115005. doi:10.1088/0960-1317/22/11/115005

Yuan, L., Hong, F., and Cheng, P. (2019). Pool boiling enhancement through a guidance structure mounted above heating surface. *Int. J. Heat Mass Transfer* 139, 751–763. doi:10.1016/j.ijheatmasstransfer.2019.05.067

Zhang, Y., Zhou, J., Zhou, W., Qi, B., and Wei, J. (2018). CHF correlation of boiling in FC-72 with micro-pin-fins for electronics cooling. *Appl. Therm. Eng.* 138, 494–500. doi:10.1016/j.applthermaleng.2018.04.053

Conflict of Interest: The authors declare that the research was conducted in the absence of any commercial or financial relationships that could be construed as a potential conflict of interest.